Science Advances
AAAS

Supplementary Materials for

Minimal-gain-printed silicon nanolaser

Byoung Jun Park *et al.*

Corresponding author: You-Shin No, ysno@konkuk.ac.kr; Myung-Ki Kim, rokmk@korea.ac.kr

Sci. Adv. **10**, eadl1548 (2024)
DOI: 10.1126/sciadv.adl1548

This PDF file includes:

Supplementary Table

Parameters	Our Device
Active volume (V_a)	$2.196\times10^{-13}\,cm^3$
Active area (A_a)	$1.830\times10^{-8}\,cm^2$
Surface recombination velocity (v_s)	$3\times10^3\ cm\cdot s^{-1}$
Bimolecular recombination coefficient (B)	$1.0\times10^{-10}\ cm^3\cdot s^{-1}$
Auger non-radiative recombination (C)	$5.0\times10^{-29}\ cm^6\cdot s^{-1}$
Confinement factor (Γ)	1.054×10^{-1}
Gain coefficient (g_0)	$3000\ cm^{-1}$
Transparency current density (n_{tr})	$1.0\times10^{18}\ cm^{-3}$
Q factor (Q)	5.7×10^3
Effective refractive index (n_{eff})	2.92
Lasing wavelength (λ)	1545.7 *nm*
Pump laser wavelength (λ_p)	976 *nm*

Table S1. Parameters used in rate equation model. The parameters used in general rate equation model.

Table S2. Emission characteristics with different duty cycles for 15 samples. This table provides a summary of the experimental conditions and key properties for 15 devices. Additionally, it includes SEM images and emission spectra for five selected devices under 10% duty cycle and high-duty/CW conditions.

Device number	Maximum duty cycle [%]	Threshold pump power[+] [μW]	Wavelength[+] [nm]	Linewidth[+] [nm]
4300-08-03[a]	100	51.8	1547.0 (1548.2)	0.67 (0.86)
4200-08-01	100	73.9	1591.1 (1592.3)	0.65 (0.74)
4800-08-03[b]	100[*]	42.1	1581.4 (1581.6)	0.65 (0.74)
4900-07-01	100[*]	101.7	1556.8 (1557.5)	0.65 (0.75)
4900-07-03	100[*]	39.8	1550.9 (1551.6)	0.68 (0.78)
4600-08-02	98	81.5	1549.4 (1550.1)	0.69 (0.73)
4200-08-02	98	82.0	1590.6 (1591.1)	0.69 (0.71)
4200-08-01	95	67.2	1585.4 (1585.9)	0.70 (0.71)
4300-08-03	90	51.9	1544.0 (1544.4)	0.68 (0.72)
4500-10-01	90	144.3	1534.2 (1534.8)	0.69 (0.70)
4600-10-03	90	77.8	1550.4 (1550.9)	0.69 (0.71)
4100-07-01	90	62.5	1528.0 (1528.5)	0.69 (0.70)
4100-09-01	70	101.9	1563.8 (1564.2)	0.68 (0.70)
4100-11-01	70	161.0	1553.0 (1553.2)	0.69 (0.68)
4200-11-02	70	98.0	1524.2 (1524.5)	0.69 (0.68)

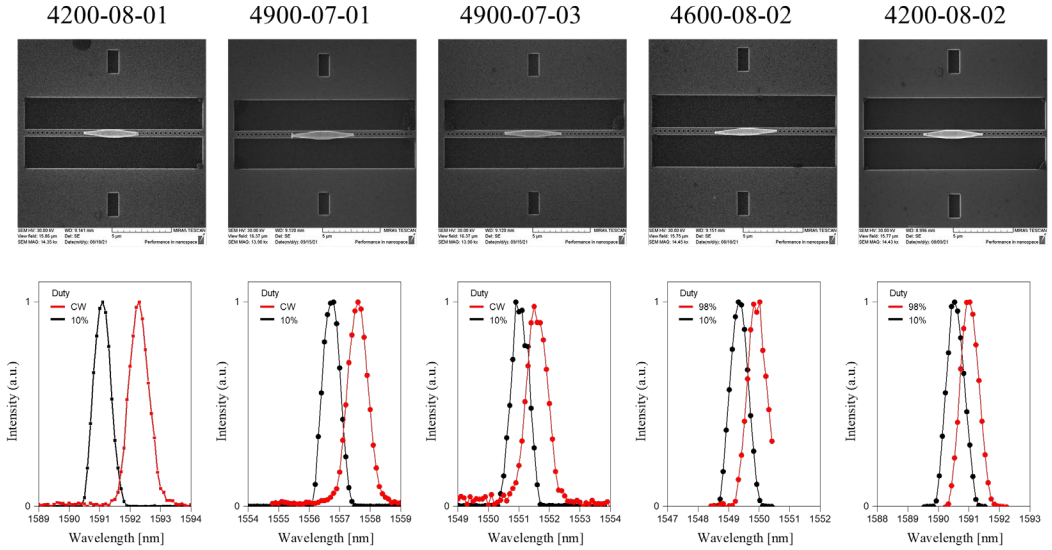

[*] The measurements were conducted at approximately 289 K.
[+] Measurements were taken at a 10% pump duty cycle, with the values in parentheses representing those measured at the maximum duty cycle for each device.
[a] This device corresponds to Figs. 4A-C.
[b] This device corresponds to Figs. 4D-F.

Supplementary Notes

Estimation of spontaneous emission factor (*β*) and internal quantum efficiency (η_i)

We use general laser rate equation for estimating both β and η_i of our gain-printed silicon nanolaser. The parameter used in the laser rate equation based on Table S1. The material parameters, such as surface recombination velocity (v_s), bimolecular recombination coefficient (B), auger non-radiative recombination (C), gain coefficient (g_0), and transparency current density (n_{tr}) of the InGaAsP wafer vary how they are made, but we could refer to values frequently used. Active volume (V_a) is calculated by measured SEM data (Fig. 3A), and other parameter confinement factor of QW (Γ), Quality factor (Q), Effective refractive index (n_{eff}), and Lasing wavelength (λ) were used as values obtained through FDTD simulation. Here, the gain of the InGaAsP is approximated in logarithmic form as follows.

$$g(n) = g_0 \log(n / n_{tr}) \tag{S1}$$

We start from the conventional rate equation as follows.

$$\frac{dn}{dt}V_a = \frac{\eta_i P_{pump}}{\hbar\omega_p} - (\frac{A_a v_s}{V_a}n + Bn^2 + Cn^3)V_a - g(n)v_g p V_a \tag{S2}$$

$$\frac{dp}{dt}V_p = g(n)v_g p V_a - \frac{pV_p}{\tau} + V_a \beta B N^2 \tag{S3}$$

The average carrier density (n) and the averaged photon density (p) can be described by S4 and S5. The frequency of pump laser (ω_p), photon lifetime (τ) and group velocity of laser mode (v_g) are given by $\omega_p = \frac{c}{\lambda_p}$, $\omega = \frac{c}{\lambda}$, $\tau = \frac{Q}{\omega}$, and $v_g = \frac{c}{n_{eff}}$, respectively. Here, the V_p means total physical volume, and we can write that $V_a / V_p \simeq \Gamma$. Therefore, the final rate equation as follow can be written (S4, S5).

$$\frac{dn}{dt} = \frac{\eta_i P_{pump}}{\hbar\omega_p V_a} - (\frac{A_a v_s}{V_a}n + Bn^2 + Cn^3) - g(n)v_g p \tag{S4}$$

$$\frac{dp}{dt} = \Gamma g(n) v_g p - \frac{p}{\tau} + \Gamma \beta B N^2 \quad \text{(S5)}$$

Based on the following rate equation, the light in-light out curve (L-L curve) near the threshold was calculated numerically. To show an equal comparison between the experimental results and the theoretical results, both results are normalized based on measured and theoretical threshold pump power (P_{th}), respectively. To get P_{th}, the g_{th} is calculated through lasing condition (S6, S7). And then n_{th} is calculated that $n_{th} = n_{tr} e^{g_{th}/g_0}$, through S8.

$$g_{th} = 1/(\Gamma v_g \tau) = g_0 \log(n_{th}/n_{tr}) \quad \text{(S6)}$$

$$P_{th} = (\frac{A_a v_s}{V_a} n_{th} + B n_{th}^{\ 2} + C n_{th}^{\ 3}) \hbar \omega_p V_a / \eta_i \quad \text{(S7)}$$

Fig. 3D shows the numerically calculated results as function of β when $\eta_i = 0.20$ with a measured P_{th} of 22.8 μW. The fitted η_i = 0.20 is in close agreement with the simulation-calculated absorption efficiency of 0.27, which includes resonance effects of the pumping beam into the structure. Finally, the best β is fitted at 0.13, and the theoretical P_{th} value is ~23.06 μW.

Performance analysis of CW Pumped Lasers

In our series of experiments, it has been consistently observed that lasers pumped with continuous-wave (CW) exhibit reduced coherence and diminished power stability compared to their pulse-pumped cases. During LL-curve measurements under pulse pumping conditions, which typically last up to an hour, we did not observe any significant degradation, indicating stable operation. Additionally, the original performance was still observed when measuring the same sample after one year. However, some degradation was noted when operating the device for more than an hour under CW conditions or high-intensity operation with peak pump power in the milliwatt range. Despite these drawbacks, we have concluded that our samples operate lasing under CW pumping for three main reasons. First, as demonstrated in Fig. S1, significant nonlinear responses in the log-log plots of the L-L curves were observed near the lasing threshold. These nonlinear behaviors indicate an abrupt transition in carrier dynamics, shifting from spontaneous to stimulated emission, which is essential process for the laser's stabilization. During the L-L curve measurements under CW pumping, however, we encountered difficulties in accurately obtaining clear output data at very low-power pumping conditions. This difficulty was due to a sharp decrease in emitted power (estimated to be below 10 pW), indicating a substantial reduction in conversion efficiency under CW pumping conditions. Second, notable shifts in the laser wavelengths near the threshold were observed, as shown in Fig. S1. In the spontaneous emission region, increasing the pumping power typically leads to a blue shift in resonance due to the band-filling effect. Above the threshold, however, the carrier density becomes clamped, halting the blueshift, and the lasing wavelength begins to redshift due to thermal effects. These shifts were consistently observed under all tested conditions: pulse pumping (Fig. S1(A)), CW pumping with thermoelectric cooling (TEC) (Fig. S1(B)), and CW pumping at room temperature (RT) (Fig. S1(C)). Notably, Figs. S1(A, B) show a minimal redshift above the lasing threshold, while Fig. S1(C) exhibits a pronounced increase. Lastly, considerable narrowing of linewidth near the threshold was observed, as shown in Fig. S2. In the case of Fig. S2(A), the linewidth quickly reaches the resolution limit of our measuring equipment. In contrast, Figs. S2(B, C) reveal relatively broader laser linewidths, a phenomenon attributed to enhanced thermal and Doppler broadening effects associated with CW pumping; nonetheless, these figures demonstrate a continuous narrowing of linewidth with increasing pump power above the threshold. We believe that further improvements, such as surface passivation of nanoblock (NB) and structural

refinement, will pave the way for the development of more robust and potent CW lasers in the future.

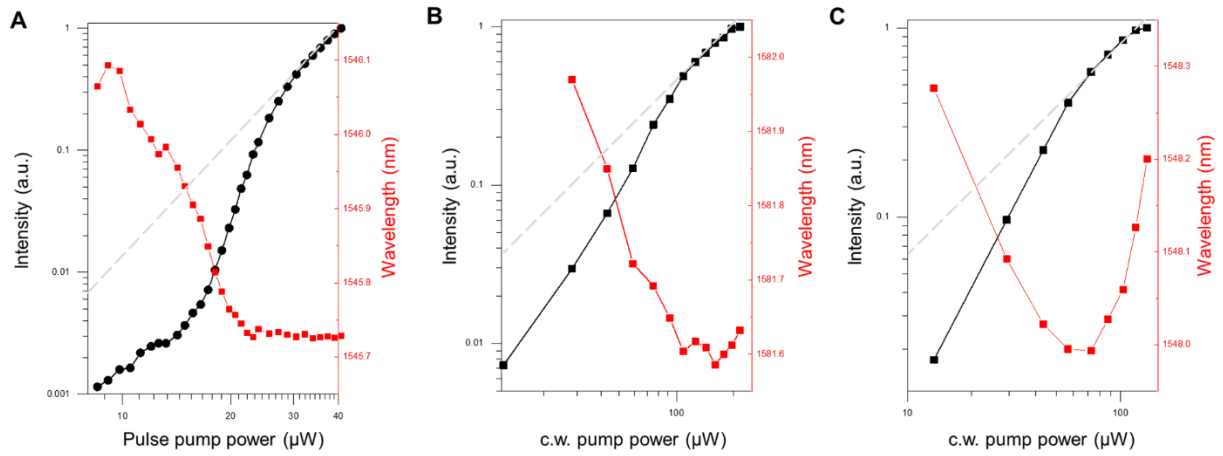

Fig. S1. Laser characteristics: L-L curves and laser wavelengths. Log-log plots of L-L curves (black) and laser wavelengths (red) under three pumping conditions: (**A**) pulse pumping (corresponding to Figs. 3C and 3F), (**B**) CW pumping with thermoelectric cooling (corresponding to Figs. 4E and 4F), and (**C**) CW pumping at room temperature (corresponding to Figs. 4B and 4C).

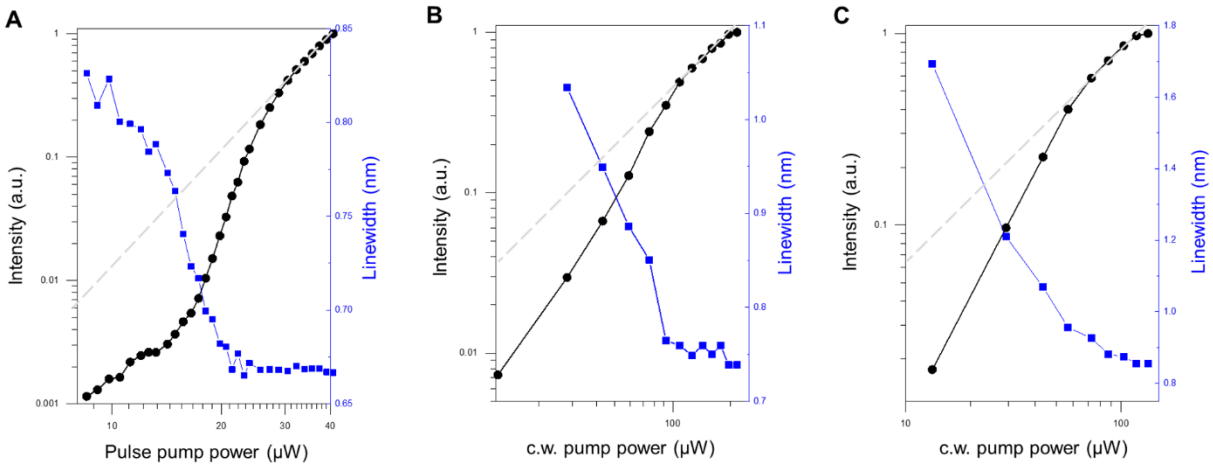

Fig. S2. Laser characteristics: L-L curves and laser linewidths. Log-log plot of L-L curves (black) and laser linewidths (blue) under three pumping conditions: (**A**) pulse pumping (corresponding to Figs. 3C and 3F), (**B**) CW pumping with thermoelectric cooling (corresponding to Fig. 4E), and (**C**) CW pumping at room temperature (corresponding to Fig. 4B).

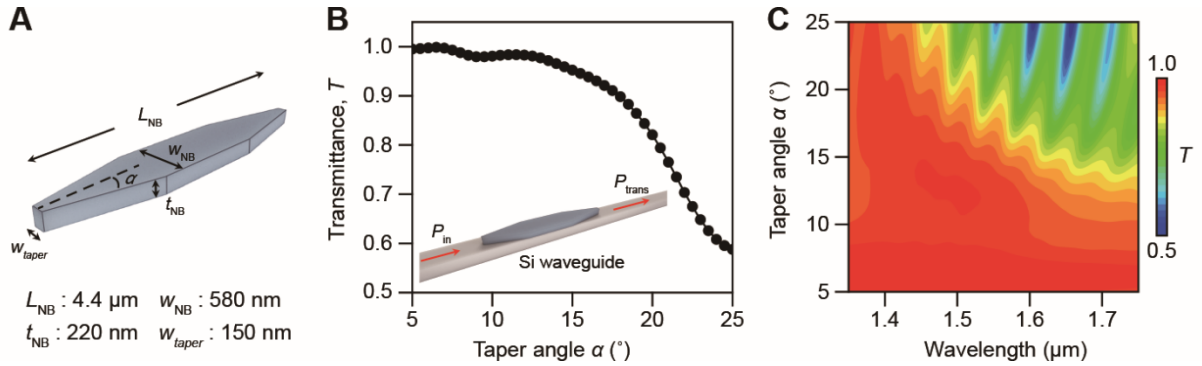

Fig. S3. Optimization of III-V NB to minimize scattering loss. (**A**) Schematic of NB. The total length (L_{NB}), width (w_{NB}), width of tapered edge (w_{taper}), and thickness (t_{NB}) of III-V NB are 4.4 μm, 580 nm, 150 nm, and 220 nm, respectively. (**B**) Transmittance as function of taper angle (α) at wavelength of 1.55 μm when NB is placed on a Si WG with a thickness and a width of 280 nm and 580 nm, respectively. (**C**) Transmittance contour plot as a function of α and wavelength.

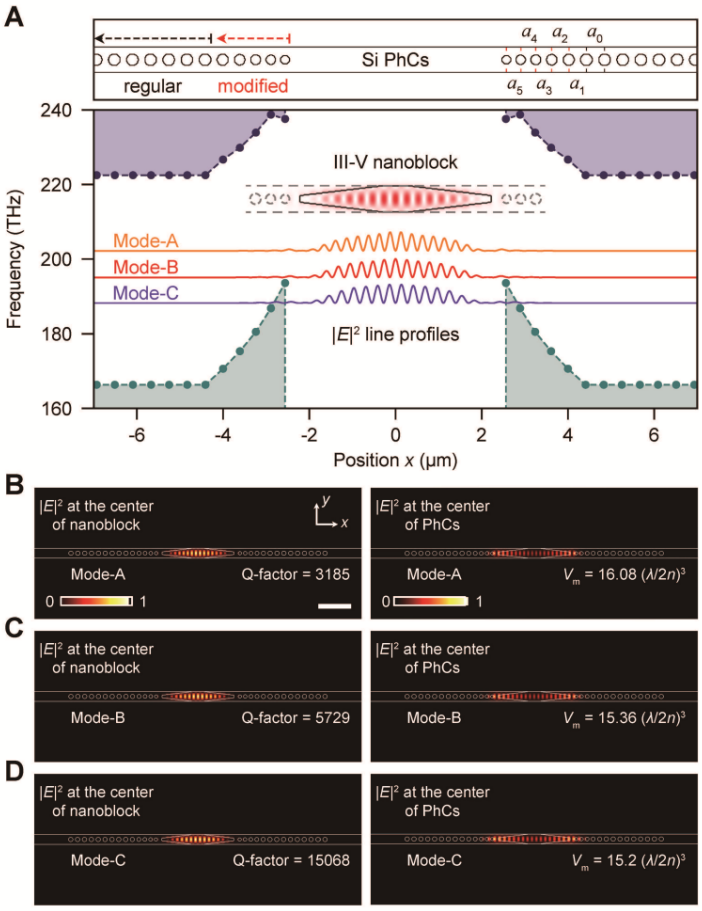

Fig. S4. Design of gain-printed Si nanolaser. (**A**) Top panel shows schematic of Si photonic crystals (PhCs). The regular and modified lattice constants of PhCs are a_0 = 420, a_1 = 400, a_2 = 380, a_3 = 360, a_4 = 340, and a_5 = 320 nm, respectively. The lower panel shows the band structure (dashed area) according to the position of the air hole. To help explain, we override electric field line profiles of Mode-A (yellow), Mode-B (red), and Mode-C (violet) along the axial direction passing through the center of the NB. The center frequency of modes is 202.2, 195.1, and 188.2 THz, respectively. Inset shows electric field profile at NB of Mode-B. (**B**) $|E|^2$ field profile of the Mode-A which the Q-factor, wavelength, and mode volumes are 3185, 1482.6 nm, and 16.08 $(\lambda/2n)^3$, respectively. The scale bar is 2 μm, *xy*-plane at NB (left), *xy*-plane at PhCs (right). (**C**) $|E|^2$ field profile of the Mode-B which the Q-factor, wavelength, and mode volumes are 5729, 1536.8 nm, and 15.36 $(\lambda/2n)^3$, *xy*-plane at NB (left), *xy*-plane at PhCs (right). (**D**) $|E|^2$ field profile of the Mode-C which the Q-factor, wavelength, and mode volumes are 15068, 1593.1 nm, and 15.2 $(\lambda/2n)^3$, *xy*-plane at NB (left), *xy*-plane at PhCs (right).

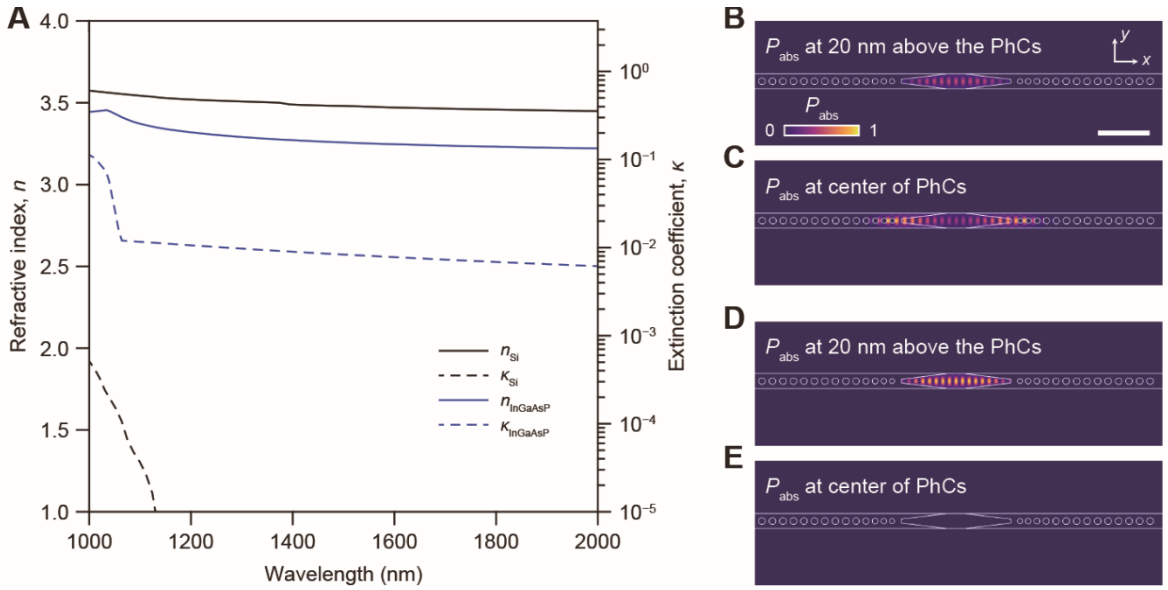

Fig. S5. Material optical properties and absorption profile at resonance wavelength. (**A**) Refractive indices of Si and InGaAsP. **B**– **C**, *xy* cut plane power absorption ($\frac{1}{2}\boldsymbol{\varepsilon_0}|\boldsymbol{E}|^2(\boldsymbol{2n\kappa})$) profile of III-V homogenous model. (**B**) 20 nm above at the interface Si PhCs and NB. The scale bar is 2 μm. (**C**) Center of loss Si PhCs. **D**– **E**, *xy* cut plane power absorption profile of III-V/Si heterogenous model, (**D**) 20 nm above at the interface Si PhCs and NB. (**E**) Center of lossless Si PhCs.

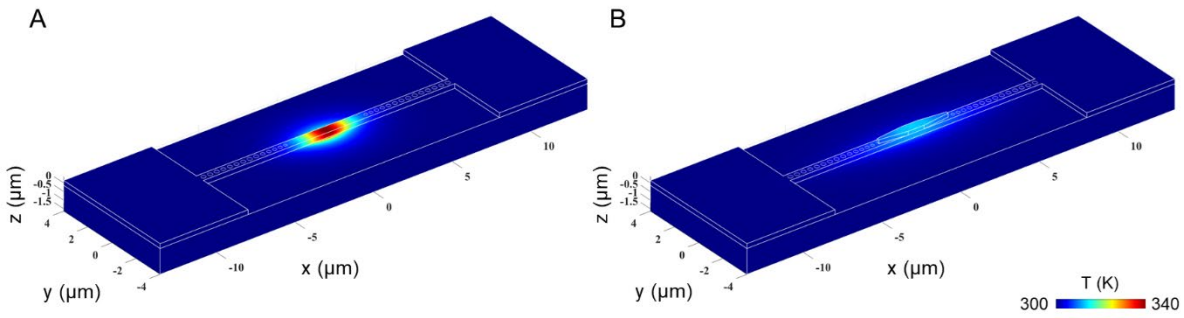

Fig. S6. Steady-state temperature distributions. Comparison of the heat dissipation capabilities of (**A**) a conventional 1D nanobeam PhC laser and (**B**) a gain-block printed Si laser.

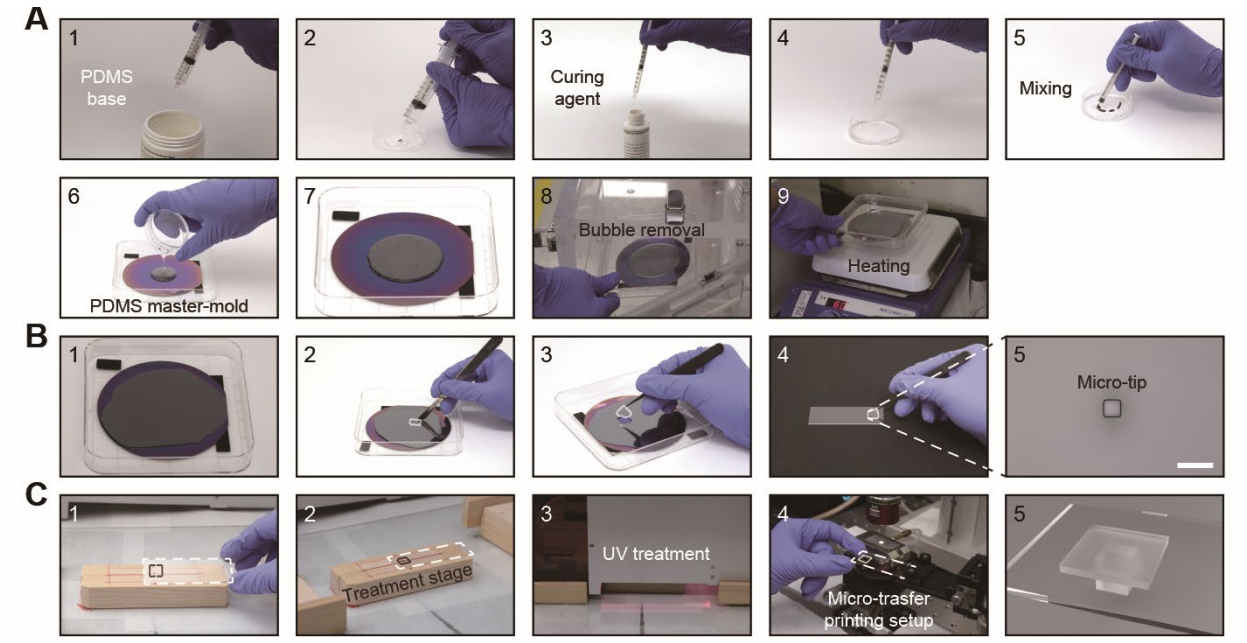

Fig. S7. PDMS micro-tip fabrication process and surface treatment steps. (**A**) Fabrication of structured PDMS: (1) draw a 5 ml PDMS base, (2) pour the PDMS base into the petri dish, (3) draw a 0.5 ml curing agent, (4) pour the curing agent into the petri dish, (5) mix the solution, (6) pour the solution on Teflon coated PDMS master-mold, (7) wait for the solution to spread, (8) remove the air bubble in desiccator, (9) heat the solution on a hot plate at 60 °C for 50 min. (**B**) Fabrication of the PDMS micro-tip: (1) hardened PDMS solution, (2) cut a piece of PDMS with a single micro-tip, (3) pick-up the piece, (4) attach to the slide glass, (5) OM image of a single micro-tip. A micro-tip size is 20 μm × 20 μm × 20 μm. The scale bar is 50 μm. (**C**) The PDMS micro-tip surface treatment steps: (1) the PDMS micro-tip on a slide glass, (2) place the slide glass on the treatment stage, (3) UV treatment for the surface modification of the PDMS micro-tip. Treatment is performed at 10 mW for 60 sec., (4) mount the slide glass on the XYZ stage, (5) schematic of the slide glass with the PDMS micro-tip attached.

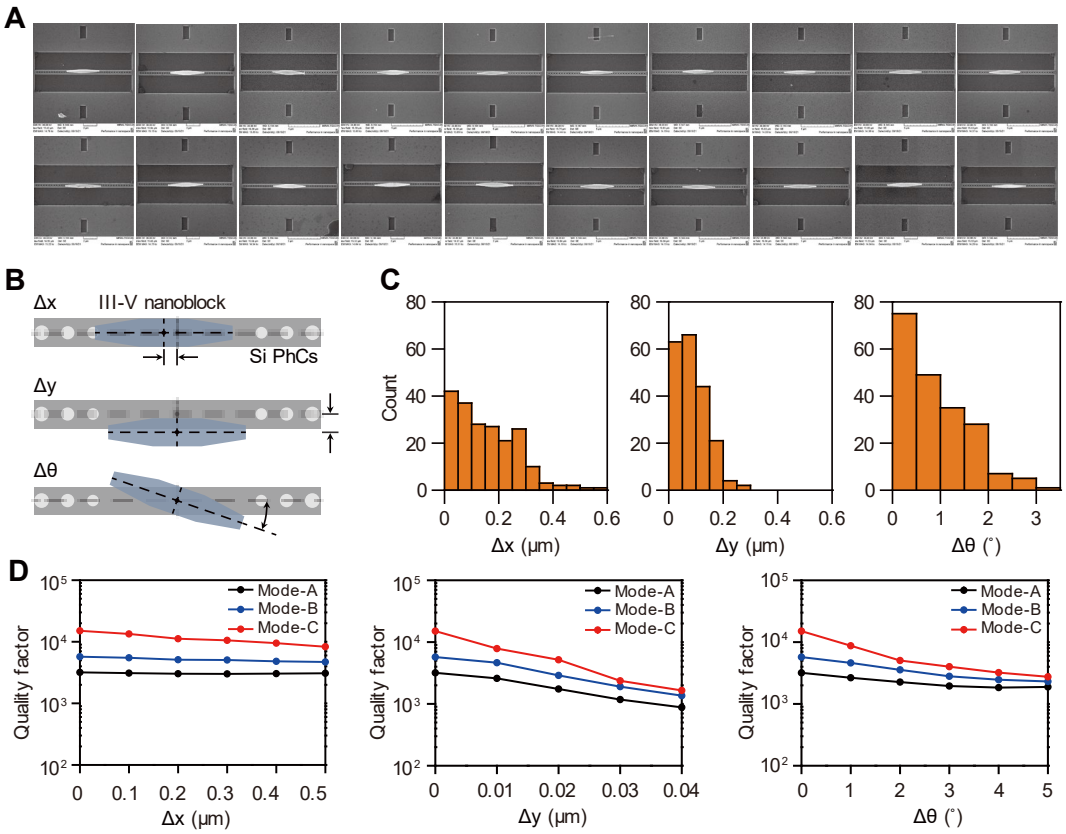

Fig. S8. Misalignment measurement of the transferred NB on the Si PhCs. (**A**) Twenty representative SEM images of the transferred NB on the Si PhCs. (**B**) Schematic representations of the horizontal (top), vertical (middle) and rotational (bottom) misalignments. (**C**) Measured misalignment distribution results for the NBs on the Si PhCs, the horizontal misalignment (left), the vertical misalignment (center), and the rotational misalignment (right). The total number of the transferred NBs implemented in the measurements was 200. (**D**) Calculated Q-factors with misalignments along the x-axis (left), y-axis (center), and angular direction (right).

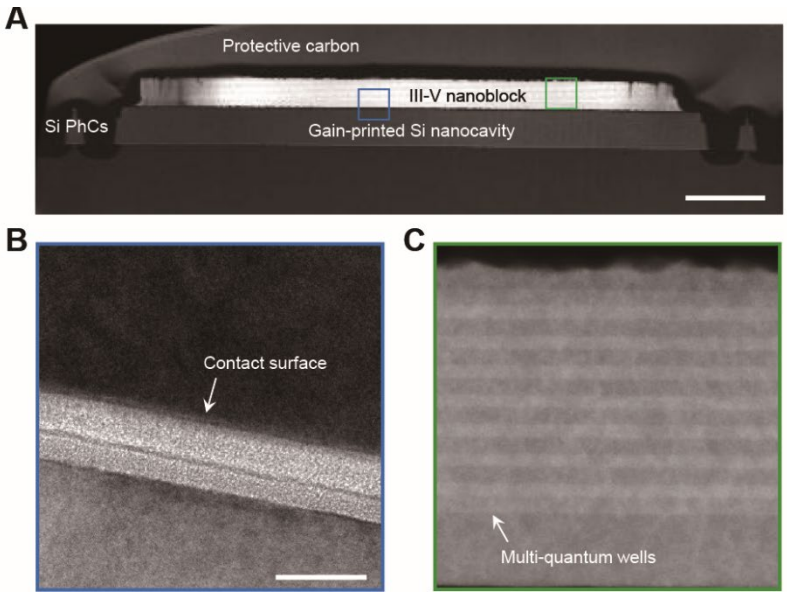

Fig. S9. Cross-sectional transmission electron microscopy (TEM) image of the gain-printed Si nanolaser. (**A**) TEM image of the gain-printed Si nanolaser, which was covered with a protective carbon layer and sliced by the focused ion-beam (FIB) etching. The TEM image shows the contact surface (blue box) and the multi-quantum wells (green box). The scale bar is 500 nm. (**B**, **C**) Magnified TEM images of the contact surface (blue box in (A)) and the multi-quantum wells (green box in (A)). The smooth interface between the III-V NB and Si PhCs reveals the high quality of a bonding. The scale bar is 50 nm.

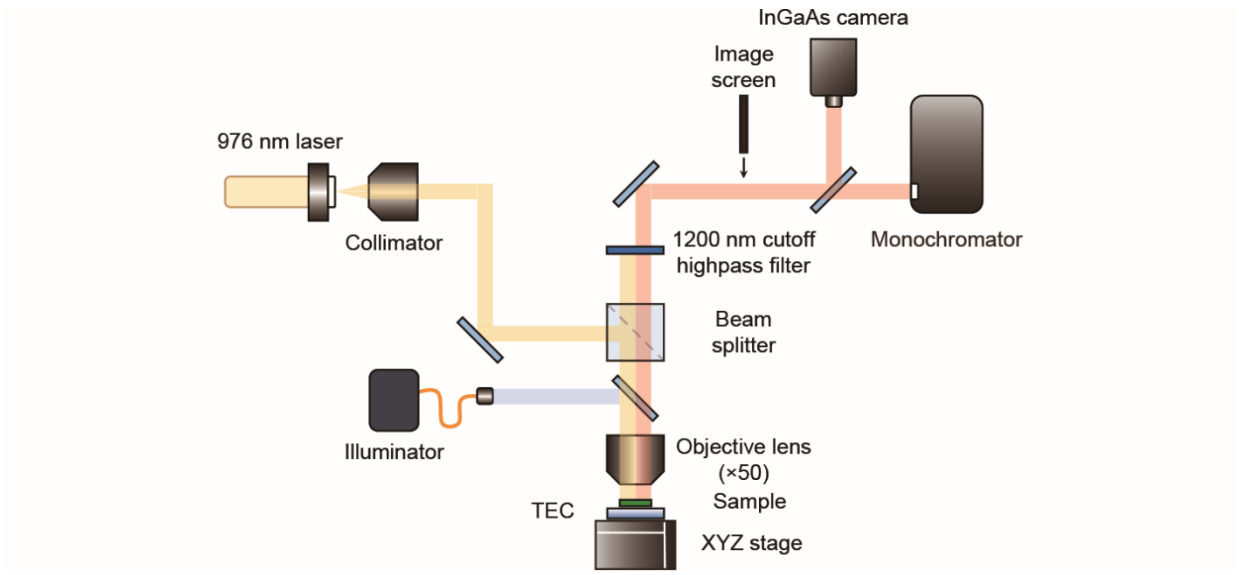

Fig. S10. Schematic of optical measurement setup. A 976 nm CW or pulse wave (1 MHz repetition rate and 100 ns or 500 ns pulse width) diode laser was used to optically pump the gain-printed Si nanolaser at room temperature. A ×50 microscope objective lens with a numerical aperture of 0.42 was used to focus the pumping beam on the laser device that was attached to a mechanically stable XYZ nanoscale translation stage and to collect the light emitted from the device. The collected light was then sent to either an NIR InGaAs camera (320HX-1.7RT 1/2 meter) for imaging or a monochromator for spectroscopic analysis. An image screen was used to measure the laser emission profile and the spectrum of the WG-coupled laser.

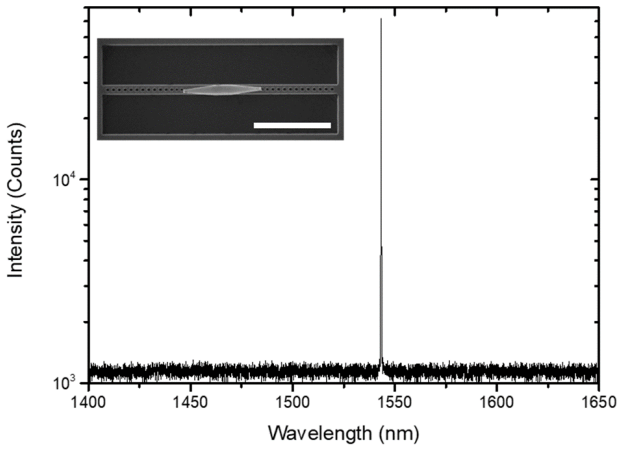

Fig. S11. Broad-range PL spectrum of Fig. 4A. Broad-range PL spectrum for the sample measured in Figs. 4A-C under pulsed pumping with a duty cycle of 10%. The inset shows an SEM image of the sample with a 5-μm scale bar.

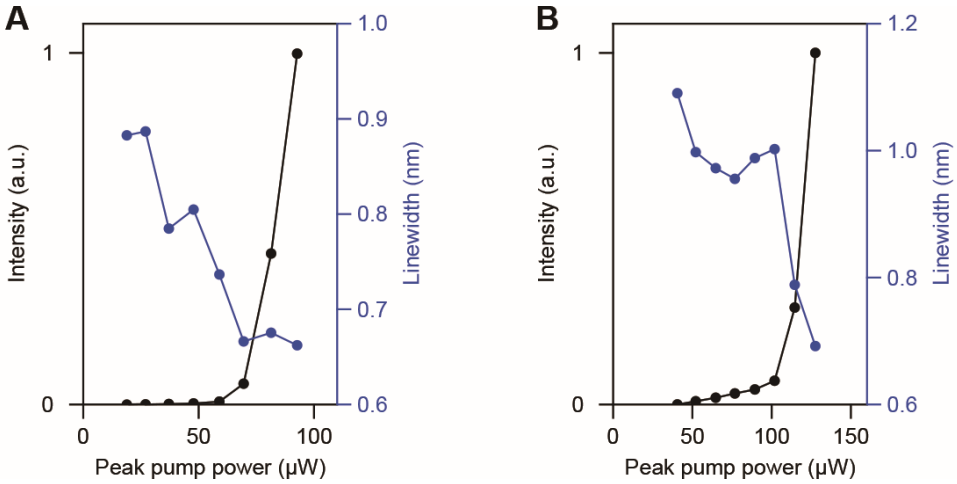

Fig. S12. L-L curve and linewidth behavior with 10% duty and 50% duty. Emission power and linewidth of laser as a function of peak pump power (P_{peak}) under RT conditions. The device used for this measurement is shown in Fig. 4A and B. The repetition rate of the incident pump laser is 1 MHz. (**A**) The device is pulsed excited with 10% duty (100 ns pulse width). The linewidth narrowed from 0.88 nm to 0.66 nm with increasing incident P_{peak}. (**B**) the device is pulsed excited with 50% duty (500 ns pulse width). The linewidth narrowed from 1.08 nm to 0.69 nm with increasing incident P_{peak}.

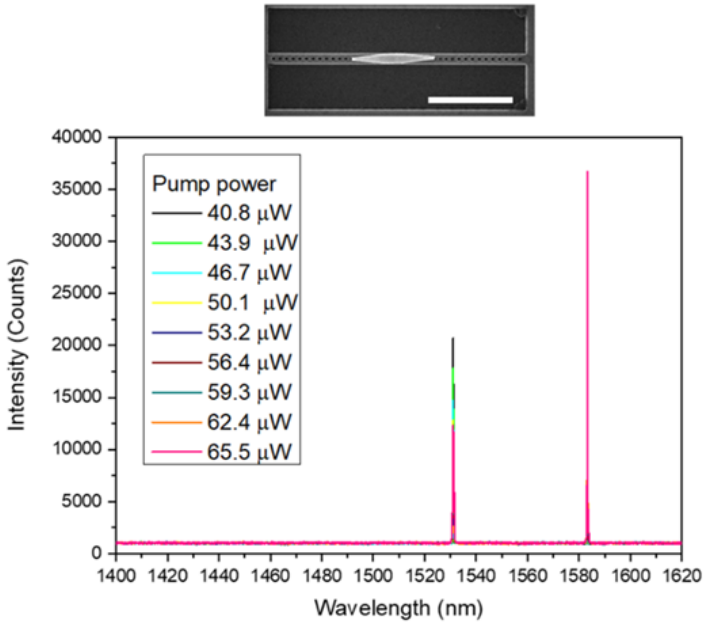

Fig. S13. Broad-range PL spectrum of Fig. 4D. Broad-range PL spectrum for the sample measured in Figs. 4D-F under pulsed pumping with a duty cycle of 10%. The inset shows an SEM image of the sample with a 5-μm scale bar.

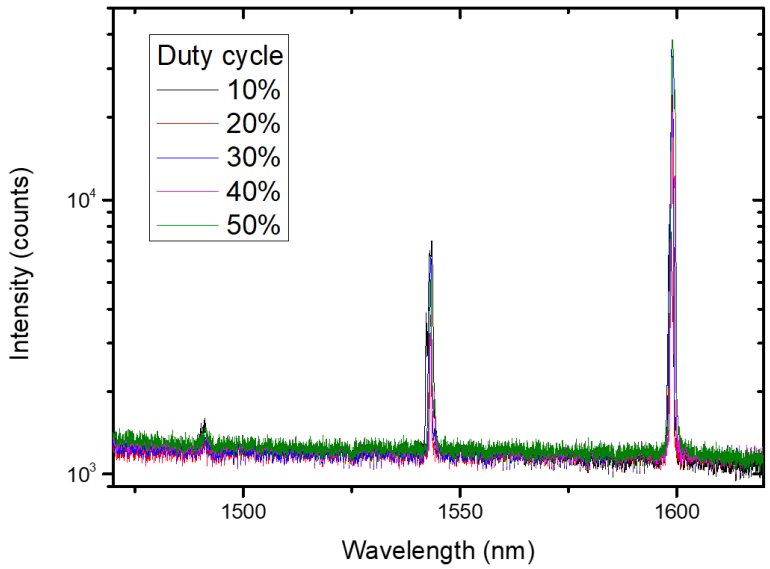

Fig. S14. **Laser spectrum with different duty cycle.** Changes in PL spectrum of the waveguide-coupled laser (as shown in Fig. 5) with variations in the duty cycle during pulse pumping.

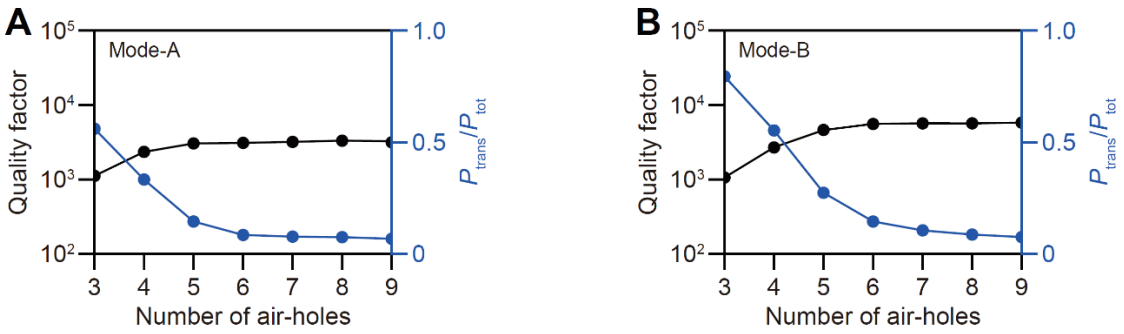

Fig. S15. Q-factor and coupling efficiency with Si WG (P_{trans}/P_{tot}) according to the number of air holes. (**A**) *Q*-factor (black-line) and coupling efficiency (blue-line) of Mode-A. (**B**) *Q*-factor (black-line) and coupling efficiency (blue-line) of Mode-B.

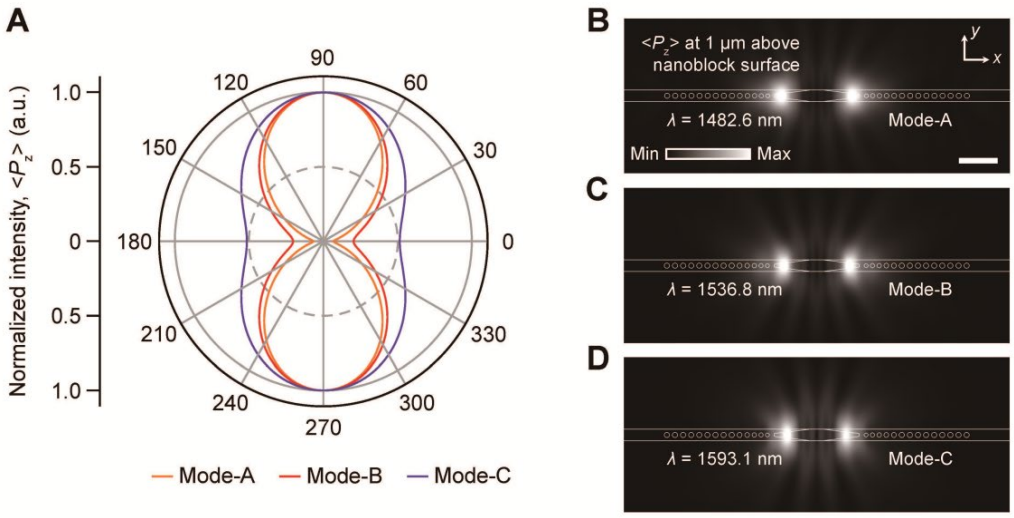

Fig. S16. Polarization characteristic and far-field <P_z> profile of gain-printed Si nanolaser. **(A)** Intensity of <P_z> in Mode-A (orange), Mode-B (red), and Mode-C (violet) as a function of the polarization angle. **B– D**, <P_z> profile of each mode calculated above 1 μm from NB. The scale bar is 2 μm. (**B**) The Mode-A with a wavelength of 1482.6 nm. (**C**) The Mode-B with a wavelength of 1536.8 nm. (**D**) The Mode-C with a wavelength of 1593.1 nm.

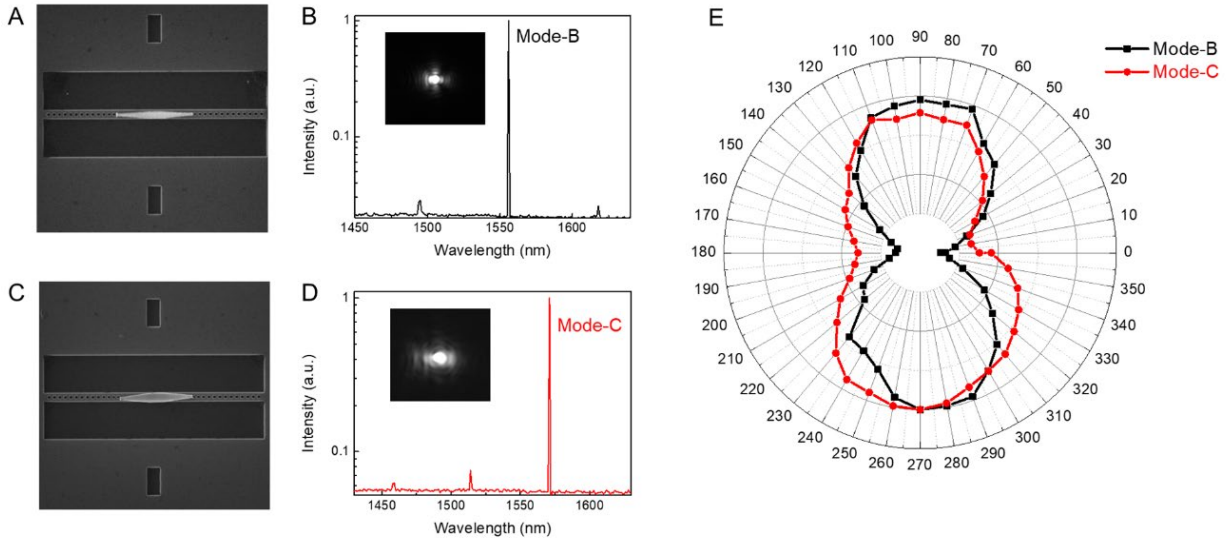

Fig. S17. Polarization characteristic measurements. (**A**, **B**) SEM image and broad-range PL spectrum with emission profile for a sample oscillating in Mode-B. (**C**, **D**) SEM image and broad-range PL spectrum with emission profile for a sample oscillating in Mode-C. (**E**) Measured polarization characteristics of both samples.

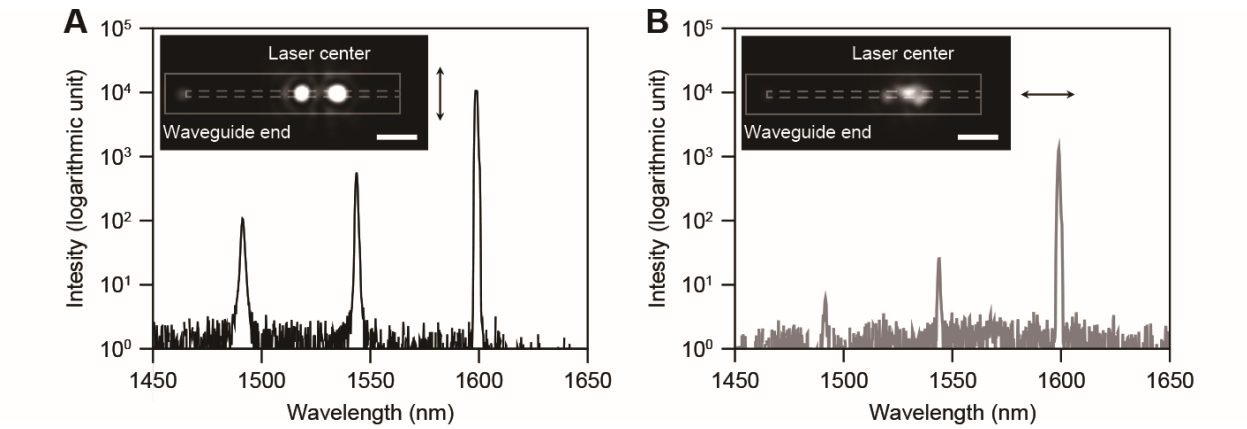

Fig. S18. Polarization characteristic of WG-coupled laser. A − B, The measured spectrum and emission profile image with different polarization. (**A**) Vertical polarization. The scale bar is 5 μm. (**B**) Horizontal polarization. The scale bar is 5 μm.